Water Column Seismic Images as Maps of Temperature Gradient

BY BARRY RUDDICK, HAIBIN SONG, CHONGZHI DONG, AND LUIS PINHEIRO

ABSTRACT. Multichannel seismic imaging of ocean water column features is a new interdisciplinary study that may become an accepted oceanographic tool in coming years. We now know that reflectors are associated with water column thermohaline fine structures such as internal waves and intrusions (on a scale of ~ 10–50 m) associated with ocean mixing, and also that the images outline larger-scale oceanographic features such as currents, water-mass boundaries, eddies, meddies, and fronts. The synopticity and detail showing the relationships between mesoscale and fine-scale features promises improved insight into the processes that cascade energy from mesoscales to mixing scales.

In order to trust a new tool, oceanographers require a quantitative understanding of how the new tool acts upon physical properties to yield a final result. We explain the basic principles of multichannel seismics, and show that the imaging process can be viewed as a filtering operation acting on the acoustic impedance field, which, on the scales that matter, is primarily (but not completely) associated with temperature variations. Synthetic seismic images show the derivative of acoustic impedance, averaged over the resolution scale of the acoustic source wavelet—they are, aside from side-lobe effects, essentially smoothed maps of temperature gradient. We use a conductivity-temperature-depth (CTD) trace from the periphery of a meddy to estimate the contribution of thermal (83%) and saline (17%) anomalies to a synthetic seismic trace, and then use multiple CTD traces from the same data set to construct a synthetic seismic image. This synthetic image compares favorably to a real seismic image of a different meddy with important differences that can be ascribed to the higher lateral resolution of the seismic technique.

INTRODUCTION

Marine multichannel seismic imaging has for decades used acoustic reflections received on a long towed hydrophone array to image structures within the solid Earth, but recently Holbrook et al. (2003) introduced a new scientific field by showing that seismic techniques can image structures within the ocean interior. Water mass fronts, currents, and boundaries; mesoscale features such as cyclones; intrathermocline eddies; meddies; and the Mediterranean Undercurrent have been imaged (Tsuji et al., 2005; Géli et al., 2005; Biescas et al., 2008; in addition, authors Pinheiro, Song, Ruddick, and colleagues have a paper in progress on detailed 2-D imaging of the Mediterranean outflow and meddies off west Iberia from multichannel seismic data). Nandi et al. (2004) and Nakamura et al. (2006) showed that the imaged reflectors correspond to oceanic thermal structures. The multichannel seismic technique uses reflections from relatively horizontal contrasts in acoustic impedance that are thinner than about 10 m. Such "fine structures" are well known in the ocean (c.f., McKean, 1974), and are associated with a variety of physical phenomena, such as internal waves, thermohaline intrusions, double-diffusive layering, mixed water patches, and vortical modes. Holbrook and Fer (2005) made quantitative inferences about internal wave energy levels near a sloping ocean bottom that may eventually link to internal wave reflection properties and near-bottom ocean mixing.

Similar to satellite images that clearly show mixing events around the edges of structures like the Gulf Stream, warm core rings, and eddies, seismic images allow us to synoptically see the relationships between fine-scale structures and the mesoscale features (like eddies) that produced them. Images that show the links from mesoscale features to fine-scale features that are associated with mixing allows hypotheses about the causes and consequences of mixing to be developed and tested in ways not previously possible. As occurred with satellite oceanography, the field of "seismic oceanography" (SO) is evolving from a curiosity to a useful and accepted tool.

Four factors make it difficult for physical oceanographers to accept SO as a viable tool: (1) the images look so different from the type of data plots we are used to (e.g., contour and waterfall plots), (2) a lack of quantitative understanding of exactly how the imaged features are related to what we would measure with a CTD, (3) seismic reflectors are treated in textbooks as sharp interfaces while

Barry Ruddick *is Professor, Department of Oceanography, Dalhousie University, Halifax, Nova Scotia, Canada.* **Haibin Song** *(hbsong@mail.iggcas.ac.cn) is Associate Professor, Institute of Geology and Geophysics, Chinese Academy of Sciences, Beijing, China.* **Chongzhi Dong** *is PhD Candidate, Institute of Geology and Geophysics, Chinese Academy of Sciences, Beijing, China.* **Luis Pinheiro** *is Associate Professor, Departamento de Geociências and Center for Environmental and Marine Studies (CESAM), Universidade de Aveiro, Aveiro, Portugal.*

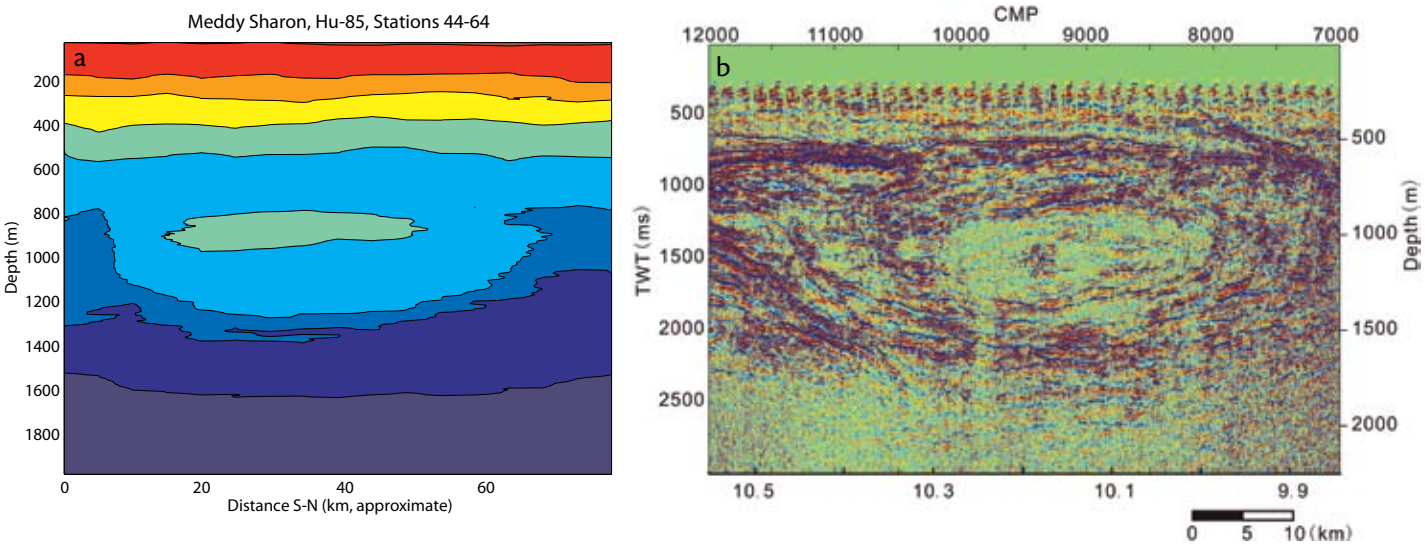

Figure 1. (a) Conventional contour plot of temperature from a CTD transect of Meddy Sharon (Armi et al., 1989). The CTD casts have a vertical resolution of a few meters, but are spaced more than 1.5 km apart. Contour interval is 2°C, with red indicating 18–20°C. (b) Seismic oceanography image from the IAM5 section on the Iberian margin during the Iberian Atlantic Margins Project showing a previously undiscovered meddy, with strong fine-structure reflectors surrounding the meddy core, and relatively few reflectors in the core. Seismic images such as this one show structures like meddies because sound reflects from the fine-scale temperature and salinity variations that are most intense near their edges. The vertical axis at left is two-way travel time (TWT)—the time required for sound to travel vertically from the surface to the reflector and back to the surface. The axis at right is the equivalent depth based on a sound velocity of 1500 m s^{-1}. Upper axis is the common midpoint (CMP) value, with 1CMP = 12.5 m. Lower x-axis is west longitude along the nearly east-west section.

ocean stratification is a combination of gradients and steps, and (4) differences in jargon specific to the fields and in the "culture" of the seismic approach, where seismic images are interpreted in terms of geologic structures on the basis of previous experience. (In fact, one of this article's authors (BR) admits to having referred—in the distant past!—to the interpretation process as "going into the back room with colored pencils and funny cigarettes, and magically emerging with a pretty picture".) We aim to bridge this cultural divide by asking: What oceanographic properties are imaged in seismic water column surveys?

In this paper, we describe the basic principles of seismic oceanography and discuss how the imaging process can be viewed as a filtering operation acting on the acoustic impedance field, which, on the scales that matter, is primarily (but not completely) associated with temperature variations. In essence, a seismic image is the convolution of reflectivity with the source wavelet, and this is nearly proportional to the vertical derivative of impedance (density times sound speed) smoothed over the resolution of the source wavelet central lobe. To a good approximation, seismic images are simply maps of dT/dz.

Figure 1a shows a conventional contour plot of the temperature structure of a Mediterranean salt lens, an eddy of warm, salty water of Mediterranean origin found in the eastern North Atlantic. Figure 1b shows a previously undiscovered meddy located through seismic imaging. Although these structures appear to be very similar in size, shape, and depth, the two images look very different, with the contour plot showing precise temperature values but not much detail, and the seismic image showing a great deal of detail but less precision. Seismic images show structures like meddies because sound reflects from the fine-scale temperature and salinity variations that are most intense near their edges.

As high-resolution synoptic images of dT/dz, seismic images are similar to Schlieren images that use lenses or parabolic mirrors to quantitatively image gradients of optical refractive index (See McEwan, 1993, for a nice application and description of the technique). The Schlieren technique has been used extensively in laboratory studies of internal waves (c.f., Mowbray and Rarity, 1967; McEwan, 1993), it is similar to the shadowgraph technique that was crucial in documenting coherent structures in turbulent flows (Brown and Roshko, 1974), and an underwater Schlieren device has been used to

image centimeter-scale mixing and double-diffusive structures in the ocean (Williams, 1974; Kunze et al., 1987) and to relate the structures to directly measured velocity, temperature, and salinity. The ability of such visualizations to persuasively induce paradigm shifts has been extensively documented, and it is possible that seismic oceanography images will do the same.

INTRODUCTION TO SEISMIC PRINCIPLES

Basics

In a seismic survey, sound is sent from a towed source, reflected from aquatic structures, and received by an array of towed hydrophones with time delays that depend on the geometry of the ray paths taken. Multichannel seismic data are acquired from a ship moving at 4–5 knots by firing an air gun array towed just behind the ship and recording the resulting acoustic wave field that has traveled through the underlying structure on a large number of hydrophones inside one or more streamers, often several kilometers long, towed about 15 m below the surface. Acoustic waves are reflected at abrupt (and not so abrupt) changes in acoustic impedance (sound velocity times density). A single reflector at depth h and a distance $x/2$ behind the source will cause sound to be reflected to a receiver at distance x behind the source, as shown in Figure 2a. (Waves in the solid Earth can be P-waves—acoustic compressional waves—or S-waves, which are elastic shear waves and do not travel through liquids; thus, water can only support P-waves that propagate with the sound velocity, c, approximately 1.5 km s^{-1}.) Fortunately, oceanic reflectors are relatively horizontal, resulting in the strongest and most coherent reflections. Using the Pythagorean theorem to calculate the diagonal travel distance, we find that the consequent time delay increases hyperbolically with the source-to-hydrophone distance, x (so-called "offset"):

$$t^2 = \frac{x^2}{c^2} + \frac{4h^2}{c^2}. \qquad (1)$$

As the source and receivers move horizontally, subsequent shots are made at intervals of 30–75 m. Acoustic waves from the subsequent shots are reflected from the same impedance change and arrive at receivers located further along the string (Figure 2b). The fact that a number of source-receiver paths give

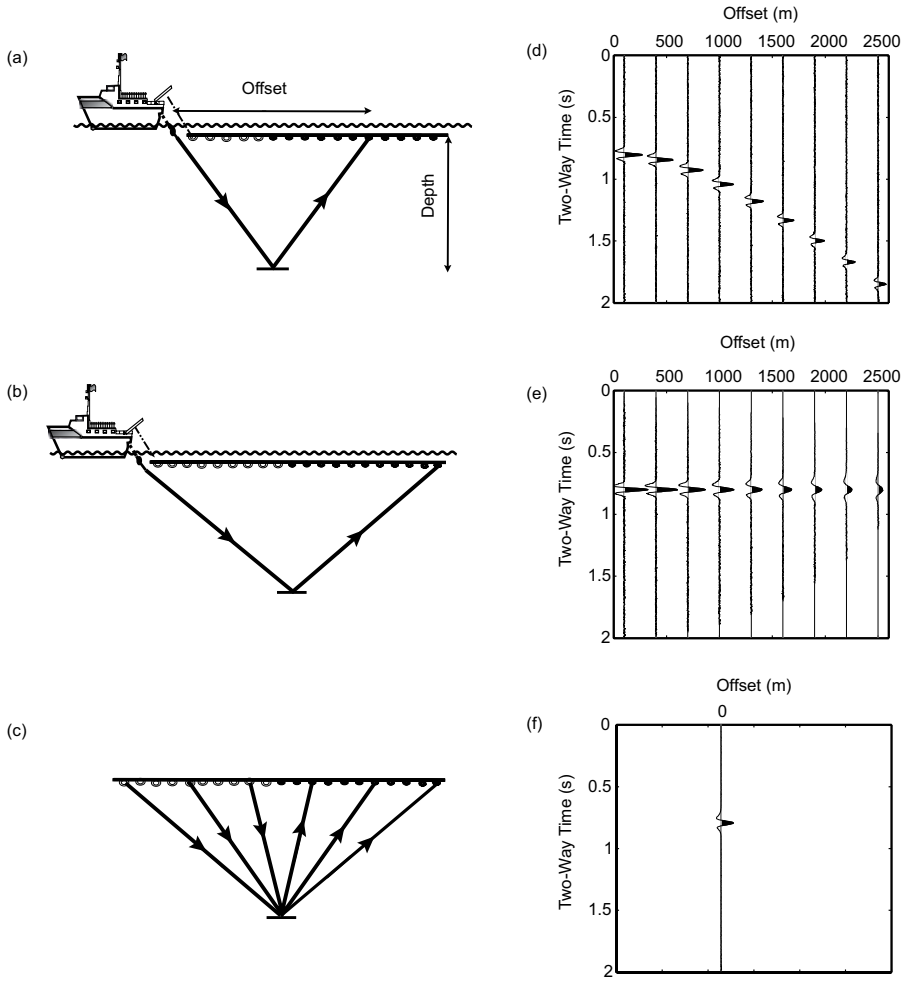

Figure 2. (a) Ship towing a sound source near the ship and an array of hydrophones behind the ship. Sound from the source is reflected at an equal angle from the (nearly horizontal) reflector at distance x/2 and reaches a hydrophone at distance x (the "offset") behind the source. (b) Diagram of a shot subsequent to the one in (a) showing how sound is reflected and then received by a hydrophone located at a larger distance from the source. In both (a) and (b), the reflector is located at or near the midpoint of the source-receiver location. (c) The set of source-receiver paths from a common midpoint (CMP) gather sound reflected from the same feature at the same physical location. (d) Schematic diagram of the traces from a CMP gather. Return versus delay time is plotted on the vertical axis, and each trace is displaced laterally an amount corresponding to the source-receiver distance for each reflection path in (c). (e) Schematic diagram of the traces from a CMP gather after normal moveout (NMO) correction, which corrects the time delay to correspond to x=0. (f) The average (or "stack") of the NMO-corrected traces from (e).

returns from each reflector with a time delay that varies hyperbolically with source-receiver spacing allows significant time-space averaging and signal/noise discrimination. This is the key to the sensitivity of the seismic method, because sets of returns that are inconsistent with the hyperbolic travel time versus distance relation, or that require an unreasonable sound velocity, can be rejected.

After each shot, the acoustic returns from each hydrophone are recorded, providing information about multiple reflectors at various depths and distances behind the source. The traces from several shots are then re-sorted into common midpoint (CMP) records, which group all traces with the same source-receiver mid-point (Figure 2c). Each reflection has a time delay that varies hyperbolically with depth h and source-to-receiver distance x (Figure 2d and Equation 1). The "normal moveout" (NMO) correction (Figure 2e) is then applied to remove the x-dependent hyperbolic curvature (Equation 1) to correct arrival times to the $x = 0$ equivalent (i.e., equivalent to a vertical traverse). Optimizing the curvature removal provides information about the sound velocity versus depth ("velocity analysis"), which gives a quantitative indication of the large-scale temperature field. The effects of sloping reflectors (called "dip"), temporal changes in reflector depth due to advection by ocean currents, and refraction due to lateral variations in sound velocity can be accounted for at this stage via a process called "migration." After performing an NMO correction with the correct velocity structure, the return from a single reflector appears in each trace at the same corrected time, allowing the traces to be "stacked" and averaged (Figure 2f). This final "stacked trace" is repeated for each CMP interval with lateral spacing of 12.5 m for this data set, but more commonly 6.25 m. The array of averaged traces from each CMP "gather" is then plotted side by side, usually using a two-color palette to show positive and negative reflector peaks. This image of the underlying reflector structure is called the "stacked section."

The vertical axis normally used on seismic sections is in "two-way travel time" (TWT), representing travel time on a vertical return path, or approximate depth below the water surface. An average sound speed of 1500 m s^{-1} is often used as a first approximation for time-to-depth conversion of seismic sections, so that 1000 ms TWT = 750-m depth. More accurate conversion from TWT to depth can be made using the velocity-depth functions derived from the hyperbolic velocity analysis. The horizontal axis is CMP, incremented by 12.5 m in the case shown here, but modern streamers more commonly yield 6.25-m CMP spacing. For oceanographic purposes, depth, latitude/longitude axes, and a distance scale are extremely useful, almost mandatory additions.

Vertical Resolution

The acoustic source in seagoing seismic systems typically consists of a number of towed strings of airguns (arrays) with carefully arranged lateral and fore-aft spacing. The guns are typically of different sizes (with smaller guns emitting higher frequencies but with less energy), and with prearranged time delays within a shot. The time lags between the various air-gun sources and the strong reflection of sound from the surface combine similarly to a ground-plane radio antenna (the sea surface being the ground plane) to give an outgoing pulse that is directed downward and backward, with significantly less energy sent to the sides. The resulting pulse, or source wavelet (Figure 3a for the IAM5 survey shown in Figure 1), is of finite width and has side lobes. The wavelet represents an approximation to the impulse response of the seismic observation/processing system; a single, sharp, horizontal reflector in an otherwise transparent medium should, in principle, show a hyperbolic pattern of returns equal to this wavelet. For the estimated IAM5 wavelet, the resolution is 22 ms, or 17 m, with significant side lobes of amplitude -0.5 (normalized relative to the central peak) at a distance of +/-18 ms (14 m) from the central peak.

Figure 3b shows estimates of the wavelet spectra, compared with the spectrum of one profile from the IAM5 data. This wavelet's energy spectrum has a broad spectral peak at f_0 = 23 Hz. The effective resolution of the wavelet (Sheriff and Geldart, 1995) is given by the Rayleigh criterion, which refers to the minimum separation needed for two sharp reflectors to be discerned (analogous to the ability of an optical system to distinguish two stars). Sheriff and Geldart (1995) state that the vertical resolution is approximately $L_0 = c/4f_0$, or one-quarter the wavelength of the dominant frequency (16 m for IAM5). Modern digital seismic systems have a significantly higher peak frequency (typically 50 Hz or even higher) with correspondingly improved (L_0 = 8 m or smaller) vertical resolution.

The wavelet spectra in Figure 3b have a minimum between 70 and 80 Hz, and

energy above this minimum is viewed as extraneous noise. Sound attenuation in water increases with frequency, resulting in minor loss of high-frequency content and slightly reduced resolution at depth. The wavelets shown are "mixed phase," leading to some imprecision about the position of reflectors. Near-perfect knowledge of the source wavelet (difficult to achieve in practice) allows the reflected traces to be deconvolved, which helps to eliminate the side-lobe effects and more precisely estimate reflector positions (Yilmaz, 2001).

Conventionally, TWT and hence depth is relative to the depth of the sound source and hydrophones (~ 15 m). The peak of the wavelet occurs at 32 ms, and this delay induces a downward reflector offset of 32 ms/1.5 m/ms = 21 m. These two effects cancel closely enough that they are ignored.

Horizontal Resolution and Migration

The images produced by standard seismic processing effectively assume that sound pulses travel as rays and are reflected with equal incidence and reflection angles from near-horizontal impedance contrasts of a scale smaller than the highest frequency in the sound source. The horizontal resolution of this technique is limited by diffraction (because the sound is band-limited) from different parts of a single reflector: a curved wave crest from the source intersects different parts of a flat reflector at slightly different times, causing phase differences between the reflection from different parts of the reflector. The first Fresnel zone radius is defined as the radius over which waves from different parts of the reflector arrive with constructive interference (their path lengths must differ by less than one quarter wavelength); it is given approximately by $R = \sqrt{\lambda h/2}$, where h is the reflector depth $\lambda = c/f_0$ and is the wavelength of sound at the wavelet peak frequency f_0 (Sheriff and Geldart, 1995, eq. 6.6a). For the source frequency (23 Hz) and depths (1500 m) shown here, the Fresnel radius is about 300 m, and higher-frequency sources improve this as $1/\sqrt{f_0}$. In two-dimensional seismic data, horizontal resolution can be partially improved by

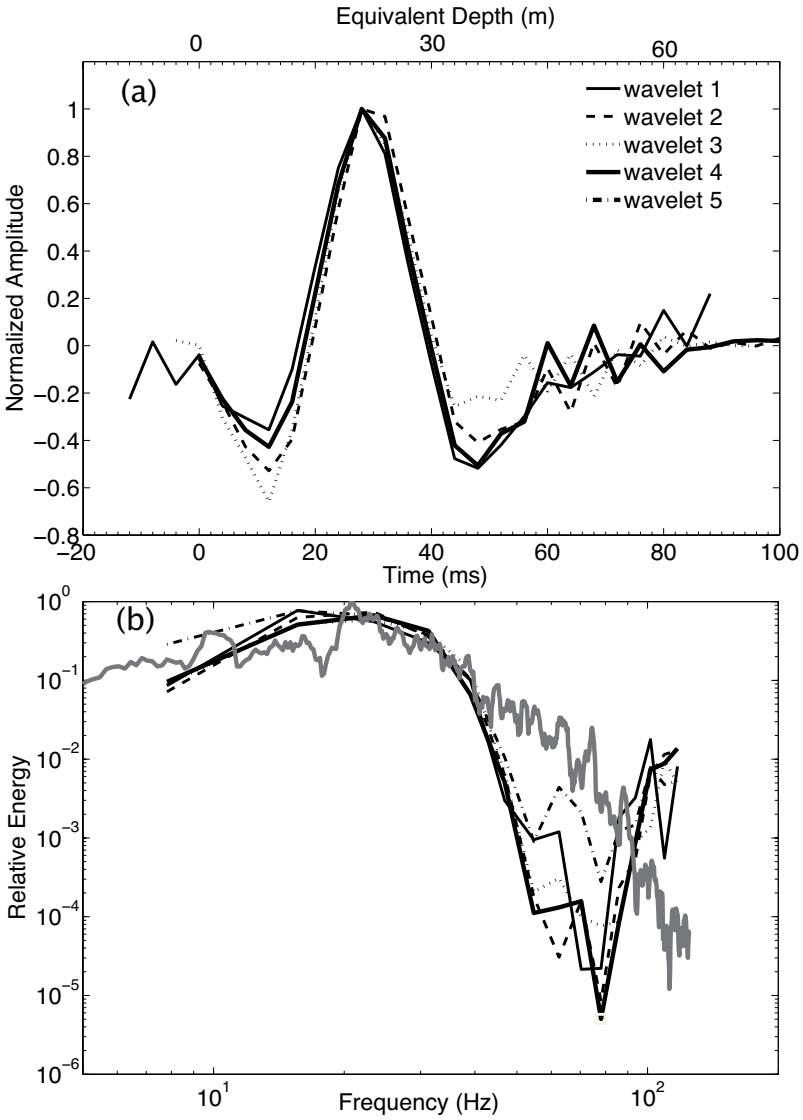

Figure 3. (a) The source wavelets from the IAM5 (Iberian-Atlantic margin) survey, estimated by the method of fourth-order cumulants (Lazear, 1993), with each estimate from different sections of data shown as a separate curve. A listener more than several hundred meters from the sound source should hear a pulse similar to the wavelet. Wavelets have been normalized and shifted so their peaks coincide. Wavelet 4 (thick line) was selected for calculations of the synthetic seismograms shown in Figures 5 and 6. (b) Wavelet spectra, using the same legend as in (a). The thick gray line is the directly measured spectrum of one seismic trace.

performing seismic migration of the data, which will collapse the Fresnel zone within the plane of the seismic section; however, this action will not account for the effects of diffraction from features outside this plane, which can only be achieved with three-dimensional data. Thus, the effective horizontal resolution of a migrated section lies between the Fresnel zone radius (~ 100 m or so) and the vertical resolution associated with the source wavelet (~ 10 m).

Migration uses Huygens' principle to allow for effects of wave crest curvature, tilted ("dipping") reflectors, and refraction due to vertically varying sound speed. Because oceanic reflectors are not strongly tilted (the steepest reflectors in Figure 1 tilt at 3°) and the sound speed variations are sufficiently weak that refraction effects are small, migration of water-column data has a relatively small effect and can make the amplitudes uncertain (Holbrook et al., 2003). However, because migration can greatly improve horizontal resolution, it can be useful to show both migrated and unmigrated seismic images, especially in situations for which horizontal resolution is critical (e.g., Holbrook and Fer, 2005). Furthermore, unlike the solid Earth, reflectors can change position during the time of passage of the hydrophone string due to horizontal or vertical advection by ocean currents, or by the vertical propagation of internal wave patterns. These effects should also be alleviated or removed by migration.

Further Reading

A modern and clear Web-based introduction to seismic concepts and methods that begins at a level similar to that discussed here, but with significantly more depth and detail, may be found at the Web page by Hardy (2001). The classic Sheriff and Geldart (1995) text gives an excellent and interesting history of the development of the seismic technique, including field techniques and equipment, and describes processing techniques in a simple and understandable way. Yilmaz (2001) describes processing techniques up to the 1980s clearly and in great detail, with many examples.

SEISMIC IMAGING AS A SMOOTHED VERTICAL DERIVATIVE

Assuming that the medium is temporally stationary on time scales of 15 minutes or so (the time it takes for a significant part of the streamer to pass a given location), the seismic image should be, to a good approximation, the convolution of the reflectivity $R(z)$ with the source wavelet $w(t)$ (also $w(z)$ with $z = c_0\, t/2$, where $c_0 = 1500$ ms^{-1}, the approximate sound speed used for conversion). We now define notation and then derive the main result: synthetic seismic images show the smoothed derivative of acoustic impedance. In the remainder of this section we allow the sound speed $c(z)$ and the density to vary with depth, causing reflections. Acoustic impedance $I(z)$ is the product of density and sound speed:

$$I(z) = \rho(z)\, c(z). \qquad (2)$$

Reflectivity $R(z)$ is calculated by assuming the ocean to be made up of uniform layers with thickness equal to the measurement quantization interval Δz, which is 2 m in the data shown below. Assuming near-vertical incidence (in practice less than 15° from normal [Sheriff and Geldart, 1995]), the reflectance between the j^{th} layer and the one immediately above is

$$R_j = \frac{I_{j+1} - I_j}{I_{j+1} + I_j} \approx \frac{\Delta I}{2I}, \qquad (3)$$

where $I_j = I(z_j)$ is the impedance of the j^{th} layer and ΔI the impedance contrast, and z_i is the depth of the j^{th} interface. Because $I_{j+1} \approx I_j + (dI/dz)(\Delta z)$, the approximation in Equation 3 is valid for small Δz. It seems odd at first to approximate a continuous medium as a sequence of layers, but the effects of smoothing by the wavelet function imply that so long as Δz is much smaller than the width of the wavelet central peak, the results are independent of Δz. We denote D as the "difference operator" sequence [...0 0 0 –1 +1 0 0 0 ...] (Bracewell, 1978) and denote convolution by $(*)$ so $\Delta I = D * I$.

Given a sequence of impedance $I(z_j)$, a synthetic seismogram is computed as the convolution of reflectivity with the source wavelet:

$$\begin{aligned} S &= w * R \\ &\approx w * \left[\frac{D * I}{2I}\right] \\ &\approx \left[w * (D * I)\right]/2I \\ &= \left[(w * D) * I\right]/2I \end{aligned} \qquad (4)$$

In the above, we used the fact that changes in impedance between two adjacent layers are small, such that the factor $(2I)$ is approximately constant on the wavelet's resolution scale, and we used the fact that convolution is a commutative operator (Bracewell, 1978; follows immediately from the Convolution Theorem).

So, to the extent that $2I$ is smooth enough that it is simply a normalizing factor, (approximately 1024 kg m^{-3} x

1500 ms^{-1}), the resulting synthetic signal is well approximated by convolving the impedance function with $w * D$, which is $(-1/2I)$ times the first difference of the source wavelet. Aside from the issues created by the side lobes of w, $w * D$ is essentially the same as viewing the acoustic impedance through a z-derivative smoothing filter that computes a smoothed derivative over scales equivalent to the width of the source wavelet.

Example: The "MATLAB Penny"

MATLAB has an excellent demonstration program in which measurements made at the US National Institute of Standards and Technology of the depth of the mold used to mint a US penny (one-cent coin) are plotted in several ways. These data, sampled on a 128 x 128 grid, are used to illustrate the effect of plotting the shape of a penny as a contour plot (Figure 4a) and with a gray-scale plot of the z-derivative (Figure 4b). Although the contour plot is more suited for reading the height of the penny at a specific point, the details of the shape are more readily discerned in the z-gradient plot—it is the fine-scale "edge" features that tell us about the shape. The z-gradient grayscale plot is similar to illuminating the penny from above Lincoln's head, making the penny look much like we are used to seeing it in real life. Similarly, for plotting high-resolution ocean temperature data, a contour plot is good for extracting quantitative information, but a grayscale derivative plot shows the detail. Contour plots are often used for oceanographic CTD data due to relatively wide station spacing, and also to indicate quantitative values of T or S. With their much higher horizontal resolution, and because seismic traces show the vertical derivative of acoustic impedance, seismic images like Figure 1b are analogous to a smoothed version of Figure 3b.

SYNTHETIC SEISMIC REFLECTIVITY PROFILE

The Role of Salinity and Density in Reflections

We saw in the previous section that the synthetic seismogram can be approximately calculated as the z-derivative of the source wavelet convolved with $I = \rho(S, T, p)c(S, T, p)$ and normalized by $2I$. Here, S is salinity, T is temperature, and p is the ambient pressure, which increases smoothly by approximately 1 decibar per meter below the surface. A perfect seismic inversion would only give us information about acoustic impedance, I, insufficient to

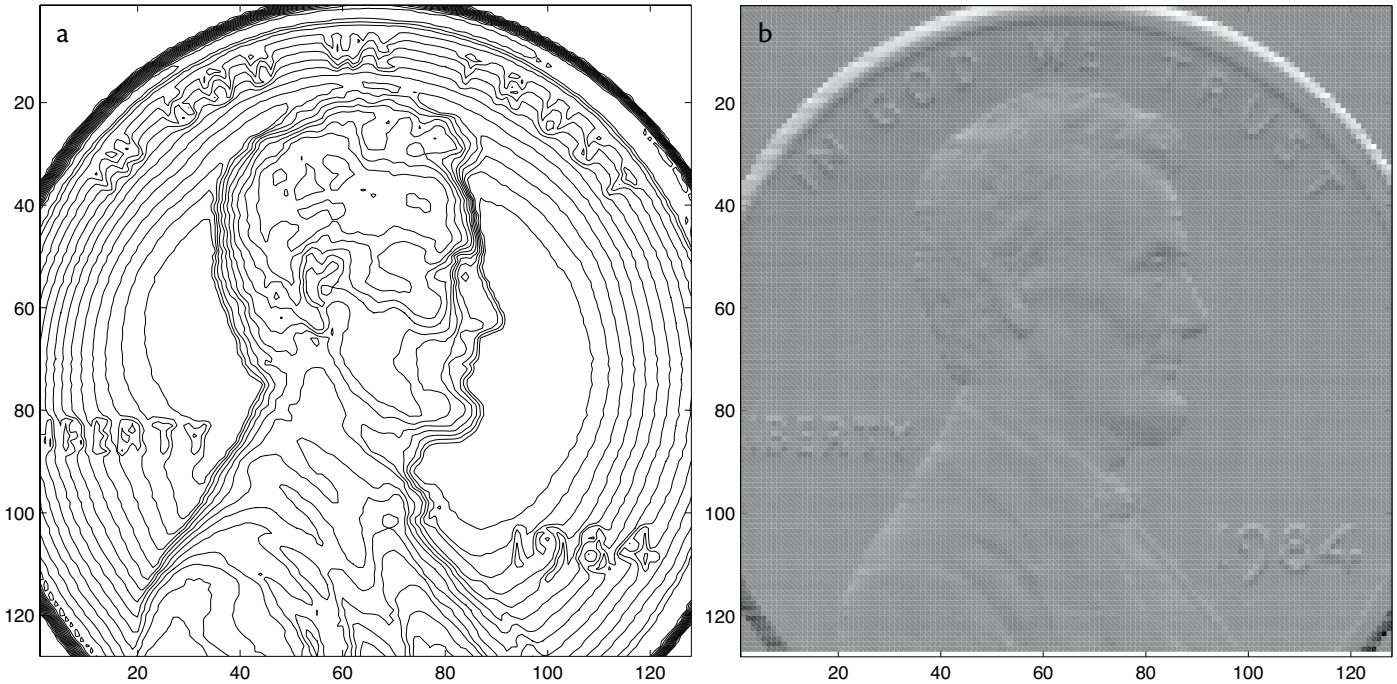

Figure 4. (a) Contour plot of the data from the MATLAB file "penny.mat." (b). Grayscale plot of the z-difference of the same data. Oceanographic data are usually plotted as in (a), while seismic images are high-resolution images of (essentially) dT/dz, analogous to (b). Notice that (b) appears like a penny lit from above, and shows details not apparent in the contour plot.

Table 1. Sound velocity and density corresponding to specific salinity and temperature values, and pressure of 1000.0 dbar, approximately equivalent to 990-m depth. Values are based on the UNESCO equations of state for density (Fofonoff, 1985) and for sound velocity (Chen and Millero, 1977). These values were calculated using the Java-based calculator {fermi.jhuapl.edu/denscalc.html}, and sound velocities were checked approximately against the equation of MacKenzie (1981).

T (°C) =		11.5	12.5
S = 35.5 psu	ρ (kg/m³) =	1031.52045	1031.31082
	c (m/s) =	1512.2	1515.7
S = 35.285 psu	ρ (kg/m³) =	1031.740374	1031.53020
	c (m/s) =	1512.6	1516.0

infer both temperature and salinity. Fortunately, acoustic impedance is much more sensitive to temperature than salinity, allowing us to approximately interpret seismic images in terms of temperature. Because p changes smoothly, we may neglect the effect of localized (wavelet-scale) changes in p and focus on the effect of variations in S and T on the synthetic seismogram. It is instructive to consider the values of density and salinity associated with specific values of S and T representative of those for which the synthetic seismogram will be calculated (see Table 1).

Increments of T (1°C) and S (0.285 psu) were chosen to be nearly density compensating, similar in ratio to oceanic thermohaline fluctuations. The increase in T causes sound velocity to increase but density to decrease, while the increase in S causes both sound velocity and density to increase. The percentage change in impedance due to temperature is about 10 times that due to salinity, but the latter should not be neglected.

Lavery et al. (2003) considered high-frequency acoustic scattering from centimeter-scale turbulent fluctuations and found that salinity fluctuations can contribute almost as strongly as temperature fluctuations. Following their approach (their Equations 12–17) and neglecting fluctuations in pressure, we write for the contribution to reflectivity:

$$\begin{aligned}\frac{\delta I}{2I} &= \frac{\delta\left(c(S,T,p)\rho(S,T,p)\right)}{2\rho c}\\ &= \tfrac{1}{2}\left(\frac{1}{c}\frac{\partial c}{\partial T}+\frac{1}{\rho}\frac{\partial \rho}{\partial T}\right)\delta T+\tfrac{1}{2}\left(\frac{1}{c}\frac{\partial c}{\partial S}+\frac{1}{\rho}\frac{\partial \rho}{\partial S}\right)\delta S\\ &= \tfrac{1}{2}(a-\alpha)\,\delta T+\tfrac{1}{2}(b+\beta)\delta S\\ &= \tfrac{1}{2}\left[\left(\frac{a}{\alpha}-1\right)+\left(\frac{b}{\beta}+1\right)R^{-1}\right]\alpha\delta T\\ &= \tfrac{1}{2}\left[\left(\frac{23.3}{2.04}-1\right)+\left(\frac{8.2}{7.5}+1\right)R^{-1}\right]\alpha\delta T\\ &= \tfrac{1}{2}\left[10.4+2.093R^{-1}\right]\alpha\delta T\end{aligned} \tag{5}$$

where

$$a=\frac{1}{c}\frac{\partial c}{\partial T}=23.3\times10^{-4}\,C^{-1}$$

$$b=\frac{1}{c}\frac{\partial c}{\partial S}=8.2\times10^{-4}\,psu^{-1}$$

$$\alpha=-\frac{1}{\rho}\frac{\partial \rho}{\partial T}=2.04\times10^{-4}\,C^{-1}$$

$$\beta=\frac{1}{\rho}\frac{\partial \rho}{\partial S}=7.5\times10^{-4}\,psu^{-1}$$

$$R=\frac{\alpha\delta T}{\beta\delta S}$$

The values of partial derivatives are taken from Table 1, appropriate to temperature of 12°C and salinity of 35.4. Here, R (we will call this the "fluctuation density ratio") indicates the dimensionless ratio of the contribution of temperature versus salinity fluctuations to density fluctuations. For density-compensated thermohaline intrusions, R~1, while for a region with a smooth T-S relation (i.e., intrusion-free with fine structure fluctuations dominated by local vertical strain and mixing events as expected from internal waves), R equals the vertical density ratio

$$R_\rho=\frac{\alpha\partial T/\partial z}{\beta\partial S/\partial z}$$

(Lavery et al., 2003). Typical values of density ratio are 1.6 in the main thermocline of the world ocean (Schmitt, 1994), and 0.1–0.3 in the diffusive-stratified Arctic and Antarctic regimes (Kelley, 2003). (Note that the density ratio is often defined as the inverse of that above in diffusively stratified waters—a confusing point.) There are also some oceanic areas that are doubly stable, with a density ratio in the range $(-\infty,0)$. Choosing the value R = 1, we see that the contribution of density-compensated salinity fluctuations to impedance variations is 2.09/(10.4+2.09) = 0.167, or nearly 17%. For R = 1.6, the contribution becomes 11%, and for R = 0.1, the contribution is 67% (however, the partial derivatives must be recalculated for cold Arctic waters). This surprisingly large effect can be easily missed due to two factors. First, because density variations are small, it might erroneously be supposed that the density terms in Equation 5 can be ignored. Second, because fluctuations in S are, in general, highly correlated with fluctuations in T (compare Figure 5a and 5b panels) in both intrusive and internal wave-dominated areas, fluctuations

in acoustic impedance look almost identical to fluctuations in temperature, even though a part comes from salinity fluctuations.

Synthetic Seismogram from a CTD Cast

For calculation of synthetic seismograms, we selected Wavelet 4 from Figure 3 and applied a fifth-order low-pass (cutoff of 87 Hz) Butterworth filter to reduce the extraneous high-frequency content. The wavelet has a spectral peak at 23 Hz corresponding to "ringing" of the sound source associated with side lobes +/- 16 m from the central peak.

Figure 5 indicates the contributions associated with variations in *S*, *T*, density, and sound velocity to a synthetic seismic trace from CTD trace 481090 of a detailed tow-yo section of Meddy Sharon (see Figure 1 of Ruddick [1992] for location). This trace is from the edge of the meddy and exhibits diffusive staircase structure (600–800 m), doubly stable meddy core (800–1050 m), and thermohaline intrusions (1050–1300 m). The thick traces show the *T*, *S*, density, sound velocity, and acoustic impedance in panels a–e. The thin traces are the temperature and other properties convolved with the derivative of the wavelet, and scaled to show the relative contributions to reflectance, then multiplied by 1000 to make the amplitudes O(1). The scaling factors have been calculated based on Equation 5 as:

(a) $\frac{1}{2}[a - \alpha] \times 10^3 = 1.06C^{-1}$,

(b) $\frac{1}{2}[b + \beta] \times 10^3 = 0.785(psu)^{-1}$,

(c) $10^3/2\rho = 10^3/(2 \text{ x } 1026\ kg\ m^{-3})$,

(d) $10^3/2c = 10^3/(2 \text{ x } 1500 \text{ m/s})$,

(e) $10^3/2\ \rho\ c = 10^3/(2 \text{ x } 1026\ kg\ m^{-3}$ x 1500 m/s), and

(f) 10^3.

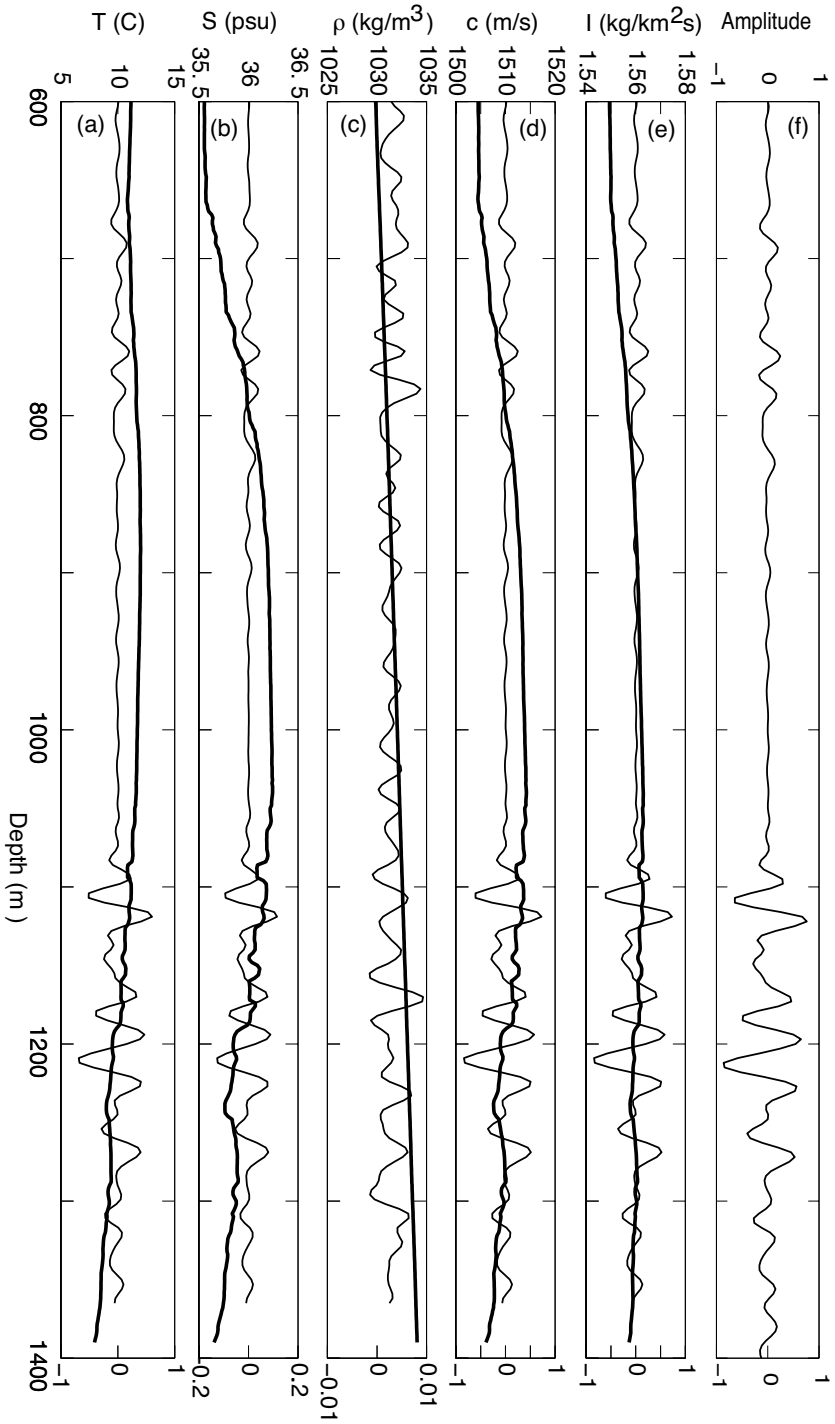

Figure 5. Oceanographic profiles versus depth (y-axis) of (thick line, upper axis scales): (a) temperature T, (b) salinity S, (c) density ρ, (d) sound velocity c, and (e) acoustic impedance I, calculated from CTD profile observations. Lower-axis scales: contribution to the synthetic seismogram (thin line, lower-axis scales) calculated by convolution of *w* with: (a) dT/dz, (b) dS/dz, (c) dρ/dz, (d) dc/dz, (e) dI/dz, and (f) R. Derivative quantities have been scaled as described in the text. The main point is that the synthetic seismogram is approximately equal to dT/dz smoothed over the scale of the source wavelet.

Because I is the product of $\rho(S,T)$ and $c(S,T)$, the four factors contributing to I are clearly not independent; thus, it makes sense to regard either (S,T) or (ρ,c) as independent variables. The contributions from S and T sum to give the calculated I, as do (separately) the contributions from ρ and c. They are simply two different ways of breaking down the contributions to I. Comparison of Figure 5 panels e and f confirms that the fluctuations in impedance are sufficiently small that the approximation used in Equation 4 is valid.

We draw several conclusions from the analyses described in this paper:

1. The synthetic seismic trace is mostly associated with fluctuations in T.
2. About 17% of the impedance contrast is associated with fluctuations in S that are strongly correlated with the T fluctuations. (The correlation between dT/dz [Figure 5a] and dS/dz [Figure 5b] is 0.9911. Although this value will vary depending on oceanic location and stratification, the correlation is relatively high over most of the world.)
3. The salinity and temperature inversions are approximately density compensating, while their associated sound speed anomalies add constructively. These are "spice anomalies" (Jackett and MacDougall, 1997) associated with lateral intrusions of water near the meddy edge and are thought to be responsible for its mixing and decay (Armi et al., 1989).
4. In comparing the contribution of density and sound velocity variations to impedance contrasts, the sound velocity variations dominate (~ 99% due to sound velocity fluctuations).
5. The reflections in the upper depth range (650–850 m) tend to have positive polarity reflectors (T and S both increasing downward) with negative reflectors occurring in the lower depth range (1050–1400 m). These depth ranges correspond to diffusive and finger-dominated intrusive zones, respectively, where Ruddick (1992) tracked intrusions laterally. The close spacing of these reflectors (~ 25-m wavelength; Ruddick and Hebert, 1988), combined with the wavelet side lobes, creates interference that makes it difficult to discern the sign of reflectors in the synthetic trace. Similarly, it is difficult to discern any systematic difference in the sign of reflectors in the seismic image of a different meddy (Figure 1b).

Nandi et al. (2004) directly measured temperature and salinity structure with expendable profilers in a Norwegian Sea seismic survey, and they were the first to document a clear association between reflectors and concurrently measured temperature variations on scales smaller than 35 m. Strong reflections in the western part of the survey were linked to temperature inversions consistent with thermohaline intrusions, while weaker reflectors in the eastern part of the survey were associated with correlated temperature and density variations consistent with internal wave strain.

It is not just internal wave strain that can cause fine structure density fluctuations to be correlated with temperature and/or salinity fluctuations. In regions dominated by thermohaline intrusions, density fluctuations are themselves weakly correlated with intrusive spice anomalies (Ruddick and Walsh, 1995). Thermohaline staircases, which have steps and well-mixed layers in T, S, and density with a fairly tight T-S relation, are found in many oceanic regions, and can be found in the upper region (700–800 m) of the meddy in Figure 1a. Finally, mixed regions produced by diapycnal mixing will cause T, S, density, and sound velocity gradient fluctuations (i.e., steps) while not producing deviations from the original T-S curve; however, these structures are generally thought to be smaller than a few meters and would be smoothed by conventional seismic imaging.

SYNTHETIC SEISMIC IMAGE FROM MEDDY SHARON

Ruddick (1992) used data from a well-resolved CTD section, including some closely spaced tow-yo observations, to trace intrusive features laterally and deduce their density changes in order to learn about their dynamics. May and Kelley (1997, 2002) greatly refined Ruddick's interpretation in terms of a more complete dynamical theory, and discussed the possibility of intrusions being tilted by ambient shear flows. We use those data, originally described in Armi et al. (1989), to create the synthetic seismogram of Figure 6. The stations are shown at the top as small tic marks; station 481070 had too many large data gaps and was omitted. Note that the position of individual stations was relatively uncertain and so we used uniform station spacing. Between each station pair, we inserted nine traces that were derived by linear interpolation of the stations on each side.

The message of Figure 6 is that the synthetic seismogram looks much like the real seismogram of the meddy in Figure 1b. The reflective features have

a similar vertical scale, appear laterally coherent (partially due to the interpolation), and outline the thermohaline structure of the meddy, showing the relatively reflection-free core, double-diffusive layering structures above and below the core, and thermohaline intrusions around the periphery, described in detail by Armi et al. (1989). The major difference between these two figures is that the real seismogram shows some steeply sloping reflectors (see the western edge in the 1200–1600-m depth range of Figure 1b) that can be tracked for hundreds of meters across isopycnals, while no such reflectors can be seen in Figure 6. We attribute this difference to the lack of horizontal resolution in the CTD section, and speculate that such reflectors would be observed with more closely spaced CTD casts. Similarly coherent, steeply sloping multiple reflectors have been observed in other seismic images of meddies (Biescas et al., 2008) and other oceanic features such as cyclonic eddies and ocean currents. The high resolution of the seismic images has documented these new oceanographic phenomena better than traditional oceanographic techniques; possible mechanisms that could create them are discussed in a paper in progress by authors Pinheiro, Song, Ruddick, and colleagues on detailed 2-D imaging of the Mediterranean outflow and meddies off west Iberia from multichannel seismic data.

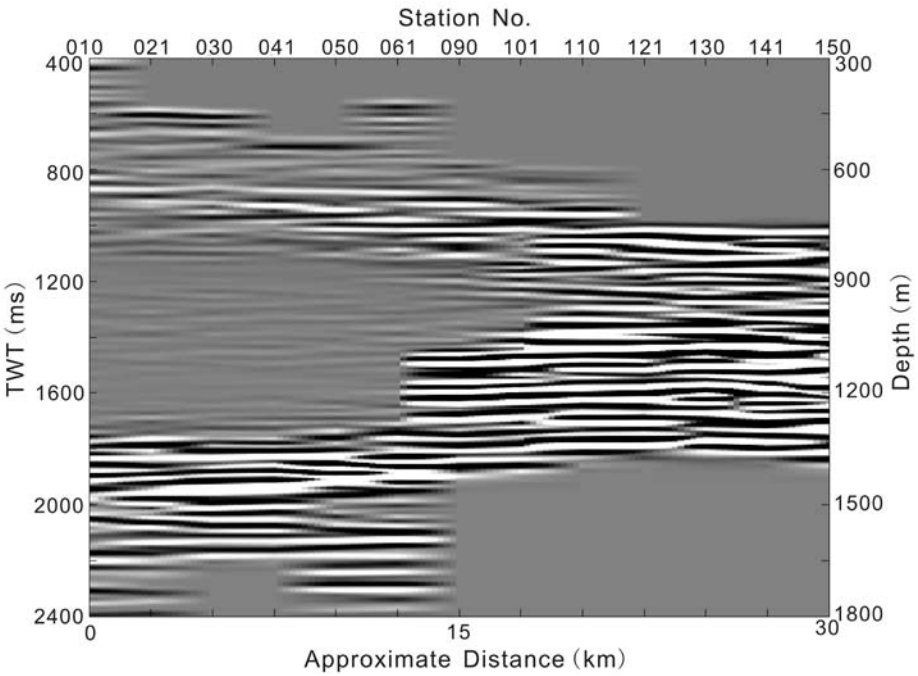

Figure 6. Synthetic seismic plot from the Meddy Sharon tow-yo section (Ruddick, 1992) and adjacent casts, stations 481010–481150 (Hebert et al., 1988). Station positions (indicated at top of plot) were separated by approximately 2 km, but are not known with sufficient accuracy to be accounted for in plotting the section. In order to replicate the high resolution of a seismic section, each station pair was augmented by 10 intermediate traces calculated by linear interpolation on adjacent stations. The synthetic seismogram looks similar to the real one of Figure 1b, although the real seismogram of Figure 1b shows multiple steeply sloping reflectors due to the superior resolution of the seismic imaging.

WHERE MIGHT SEISMIC OCEANOGRAPHY LEAD?

Seismic oceanography uses low frequency (1–200 Hz) sound that is emitted from air guns, reflected from oceanic structures, and received on a towed array of hydrophones to image the water column with ~ 10-m resolution. Seismic water column imaging can be viewed as a filter acting on the acoustic impedance field, which, on the scales that matter, is primarily (but not completely) associated with temperature variations. Careful consideration of the contributions of T and S variations to impedance contrasts suggests that temperature variations dominate but that salinity variations strengthen impedance contrasts by O(10%). Salinity variations are highly correlated with temperature variations on the scales that reflect sound, and so they enhance but do not change the appearance of reflectors. Seismic images of the water column are therefore primarily images of vertical temperature gradient smoothed over the resolution scale of the seismic source wavelet, typically ~ 10 m.

As images of temperature gradient, seismic images are closely analogous to Schleiren images, which revolutionized laboratory fluid dynamics by showing how small-scale details relate to larger structures. The most exciting promise of seismic oceanography is that synoptic visualization of features such as eddies and their associated fine structures allows the relationship between them to be explored in a new way. Because mixing generally passes energy from mesoscale features to fine scales, then to turbulence and molecular dissipation, this visualization tool gives us a new way to look at important stages in the energy cascade.

Multiple closely spaced CTD traces from the Meddy Sharon data set were used to construct a synthetic seismic image (Figure 6) that compares very favorably to a real seismic image (Figure 1b), and with other seismic images of meddies. In addition, seismic images of meddies and other features show multiple, coherent, steeply sloping reflectors that can be clearly tracked because of the high resolution of this technique. Seismic imaging revealed these new features, which have yet to be fully explained.

Current efforts in seismic oceanography are divided among the following activities:

1. Analysis of existing "legacy" data that have already been collected for geophysical reasons. It is crucial to find and use conventional oceanographic observations to support the interpretation of the imaged features.
2. Collecting concurrent physical oceanographic and seismic observations, either as add-ons to existing seismic surveys (e.g., Greenan et al., 2008) or as experiments designed to compare seismic and conventional observations of oceanographic phenomena (Hobbs, 2007).
3. Numerical and theoretical explorations of enhanced analysis techniques. These techniques use modeled oceanic impedance structures of varying complexity to generate synthetic seismic data and explore the effects of different processing algorithms. Wood et al. (2008) applied full waveform inversion (a computationally intensive and accurate technique) to synthetic and real seismic data to recover the oceanic temperature profile within 0.5°C. Inversions of synthetic seismic data show the technique can resolve oceanic fine structure at the 5-m vertical scale with arbitrary accuracy (i.e., exceeding the normal Rayleigh resolution), although accuracy and resolution in real data depend on having a broadband frequency source and accurate knowledge of the source wavelet, an excellent signal/noise ratio, and other real-world factors. Wood et al. (2008) envision the possibility that traditional (sparse but accurate) profile measurements of T and S could be augmented with seismic data, resulting in highly resolved and accurate hydrographic images.

Someday in the future, oceanographers may set out on oceanographic vessels equipped with purpose-built SO systems that could be easily deployed while underway. This system would likely have a broadband sound source with lower peak power than conventional geophysical sources. To minimize impact on living organisms, it would emit energy over time rather than as an intense pulse. The hydrophone array would be shorter than conventional geophysical streamers (the near hydrophones are associated with near-vertical reflections, which are the strongest ones, yield more coherent reflections, and give a "sharper" image), and it would deploy automatically from the stern of the vessel as it gets underway. As computers become more powerful, seismic images would be generated in the shipboard lab during transects, giving immediate guidance for further scientific investigation.

ACKNOWLEDGEMENTS

We thank Steve Holbrook, Richard Hobbs, and three anonymous reviewers for truly valuable suggestions. This research project is part of the European funded GO Project (Geophysical Oceanography - FP6-2003-NEST 15603) for which the authors warmly acknowledge support and collaborations within the research team. HB Song's research was co-financially supported by the National Major Fundamental Research and Development Project of China (No. 2007CB411704, G20000467) and by the CESAM Associated Laboratory of the University of Aveiro. We thank Dan Herold for the first suggestion to use the processing scheme adopted, and Dirk Klaeschen for the use of his code to perform the adaptive subtraction of the estimated direct wave arrivals. BRR wishes to thank Steve Holbrook and Ramzi Mirshak for helpful discussions, and acknowledges the support of Canada's Natural Sciences and Engineering Research Council. The seismic line IAM-5 was acquired in the frame of the Iberian Atlantic Margins (IAM) Project of the EU Joule Programme (EEC Contract #JOU2-CT92.O177).

REFERENCES

Armi, L., D. Hebert, N. Oakey, J. Price, P. Richardson, T. Rossby, and B. Ruddick. 1989. Two years in the life of a Mediterranean salt lens. *Journal of Physical Oceanography* 19:354–370.

Biescas, B., V. Sallares, J.L. Pelegrı, F. Machın, R. Carbonell, G. Buffett, and J.J. Danobeitia. 2008. Imaging meddy finestructure using multichannel seismic data. *Geophysical Research Letters* 35, L11609, doi:10.1029/2008GL033971.

Bracewell, R.N. 1978. *The Fourier Transform and its Application*. Second edition, McGraw-Hill Book Co., New York, 616 pp.

Brown, G.L., and A. Roshko. 1974. On the density effects and large structure in turbulent mixing layers. *Journal of Fluid Mechanics* 64:775–816.

Chen, C.T., and F.J. Millero. 1977. Speed of sound in seawater at high pressures. *Journal of the Acoustical Society of America* 62(5):1,129–1,135.

Fofonoff, N. P. 1985. Physical properties of seawater: A new salinity scale and equation of state of seawater. *Journal of Geophysical Research* 90(C2):3,332–3,342.

Géli, L., B. Savoye, X. Carton, and M. Stéphan. 2005. Seismic imaging of the ocean internal structure: A new tool in physical oceanography. *Eos, Transactions of the American Geophysical Union* 86(2):15.

Greenan, B., M. Nedimovic, K. Louden, R. Mirshak, B. Ruddick, and J. Shimeld. 2008. ROSE – Reflection Ocean Seismic Experiment. *Bulletin of the Canadian Meteorological and Oceanographic Society* 36(2):43–50.

Hardy, R. 2001. Basic Seismic Processing for Interpreters (Revised August 2008). http://www.xsgeo.com/course/contents.htm (accessed January 10, 2009).

Hebert, D., N. Oakey, B. Ruddick, L. Armi, J. Price, P.L. Richardson, and T. Rossby. 1988. CTD data collected during the survey of a Mediterranean salt lens. *Canadian Data Report of Hydrography and Ocean Sciences No. 61*, Fisheries and Oceans Canada, Ottawa, 379 pp.

Hobbs, R. 2007. PROJECT: GO–Geophysical Oceanography: A new tool to understand the thermal structure and dynamics of oceans. *European Region Newsletter* 2:7. Available online at: http://www.aapg.org/europe/newsletters/2007/06jun/06jun07europe.pdf (accessed January 15, 2009).

Holbrook, W.S., P. Paramo, S. Pearse, and R.W. Schmitt. 2003. Thermohaline fine structure in an oceanographic front from seismic reflection profiling. *Science* 301:821–824.

Holbrook, W.S., and I. Fer. 2005. Ocean internal wave spectra inferred from seismic reflection transects. *Geophysical Research Letters* 32, L15604, doi:10.1029/2005GL023733.

Jackett, D.R., and T.J. McDougall. 1997. A neutral density variable for the world's oceans. *Journal of Physical Oceanography* 27: 237–263.

Kelley, D.E., H.J.S. Fernando, A.E. Gargett, J. Tanny, and E. Ozsoy. 2003. The diffusive regime of double-diffusive convection. *Progress in Oceanography* 56:461–481.

Kunze, E., A.J. Williams III, and R.W. Schmitt. 1987. Optical microstructure in the thermohaline staircase east of Barbados. *Deep-Sea Research Part A* 34:1,697–1,704.

Lavery, A., R.W. Schmitt, and T.K. Stanton. 2003. High-frequency acoustic scattering from turbulent oceanic microstructure: The importance of density fluctuations. *Journal of the Acoustical Society of America* 114(5):2,685–2,697.

Lazear, G.D. 1993. Mixed-phase wavelet estimation using fourth-order cumulants. *Geophysics* 58:1,042–1,051.

MacKenzie, K.V. 1981. Nine-term equation for sound speed in the ocean. *Journal of the Acoustical Society of America* 70:807–812.

May, B.D., and D.E. Kelley. 1997. Effect of baroclinicity on double-diffusive interleaving. *Journal of Physical Oceanography* 27:1,997–2,008.

May, B.D., and D.E. Kelley. 2002. Contrasting the interleaving in two baroclinic ocean fronts. *Dynamics of Atmospheres and Oceans* 36:23–42.

McEwan, A.D. 1993. The kinematics of stratified mixing through internal wavebreaking. *Journal of Fluid Mechanics* 128:47–57.

McKean, R.S. 1974. Internal wave measurements in the presence of fine-structure. *Journal of Physical Oceanography* 94: 200–213.

Mowbray, D.E., and B.S.H. Rarity. 1967. A theoretical and experimental investigation of the phase configuration of internal waves of small amplitude in a density stratified liquid. *Journal of Fluid Mechanics* 28:1–16.

Nakamura, Y., T. Noguchi, T. Tsuji, S. Itoh, H. Niino, and T. Matsuoka. 2006. Simultaneous seismic reflection and physical oceanographic observations of oceanic fine structure in the Kuroshio extension front. *Geophysical Research Letters* 33, L23605, doi:10.1029/2006GL027437.

Nandi, P., W.S. Holbrook, S. Pearse, P. Paramo, and R.W. Schmitt. 2004. Seismic reflection imaging of water mass boundaries in the Norwegian Sea. *Geophysical Research Letters* 31, L23311, doi:10.1029/2004GL02135.

Ruddick, B.R. 1992. Intrusive mixing in a Mediterranean salt lens: Intrusion slopes and dynamical mechanisms. *Journal of Physical Oceanography* 22(11):1,274–1,285.

Ruddick, B.R., and D. Hebert. 1988. The mixing of Meddy "Sharon." Pp. 249–262 in *Small-Scale Turbulence and Mixing in the Ocean*, J.C.J. Nihoul and B.M. Jamart, eds, Elsevier Science.

Ruddick, B., and D. Walsh. 1995. Observations of the density perturbations which drive thermohaline intrusions. Pp. 329–334 in *Double-Diffusive Convection,* A. Brandt and H.J.S. Fernando, eds, American Geophysical Union, Washington, DC.

Schmitt, R.W. 1994. Double diffusion in oceanography. *Annual Review of Fluid Mechanics* 26:255–285.

Sheriff, R.E., and L. P. Geldart. 1995. *Exploration Seismology*, 2nd ed. Cambridge University Press, 592 pp.

Tsuji, T., T. Noguchi, H. Niino, T. Matsuoka, Y. Nakamura, H. Tokuyama, S. Kuramoto, and N. Bangs. 2005. Two-dimensional mapping of fine structures in the Kuroshio Current using seismic reflection data. *Geophysical Research Letters* 32, L14609, doi:10.1029/2005GL023095.

Williams, A. J. 1974. Salt fingers observed in the Mediterranean outflow. *Science* 185:941–943.

Wood, W.T., S. Holbrook, M.K. Sen, and P.L. Stoffa, 2008. Full waveform inversion of reflection seismic data for ocean temperature profiles. *Geophysical Research Letters* 35, L04608, doi:10.1029/2007GL032359.

Yilmaz, O. 2001. *Seismic Data Analysis: Processing, Inversion, and Interpretation of Seismic Data*, vol. 2, 2nd ed. Investigations in Geophysics No. 10, Society for Exploration Geophysics, Tulsa, OK, 2,027 pp.